

Dynamical bicontinuous networks from 3D active phase separation

Paarth Gulati^{1,4†}, Liang Zhao^{1†}, Michio Tateno², Omar A. Saleh^{1,2,3},

Zvonimir Dogic^{1,3}, M. Cristina Marchetti^{1,3*}

¹Department of Physics, University of California, Santa Barbara, CA 93106, USA

²Department of Materials, University of California, Santa Barbara, CA 93106, USA

³Interdisciplinary Program in Quantitative Biosciences, University of California, Santa Barbara, CA 93106, USA

⁴Department of Physics, Emory University, Atlanta, Georgia 30322, USA

*Corresponding author. Email: cmarchetti@ucsb.edu

†These authors contributed equally to this work.

We study phase separation between coexisting active and passive fluids in three-dimensions, using both numerical simulation and experiments. Chaotic flows of the active phase drive giant interfacial deformations and cause the co-existing phases to interpenetrate, generating a continuously reconfiguring bicontinuous steady-state morphology that persists over the lifetime of the active fluid. We demonstrate how activity controls the structure of the bicontinuous network. Quantitative analysis reveals the dominance of dynamical steady-state sheet-like interfaces, in marked difference from the transient bicontinuous structures observed in passive liquid-liquid phase separation, where saddle-like surfaces dominate. These results demonstrate how active stresses suppress the coarsening dynamics of conventional phase separation, generating steady-state reconfigurable morphologies not accessible with conventional surface-modifying agents or through quenching of transient phase separated structures.

1 Introduction

Bicontinuous structures consist of two distinct interconnected and interpenetrating phases, where each phase spans the entire subvolume. By maximizing the interfacial area while retaining connectivity, bicontinuity underpins vital mechanical and chemical functionalities in diverse natural and synthetic systems. An example from living matter is the endoplasmic that spans the cell interior. This bicontinuous structure performs protein synthesis, lipid production, and molecular transport on its interconnected membrane, while the bone trabecular lattice balances the mechanical strength of the mineralized struts with nutrient transport through vascularized marrow channels (1–4). In synthetic systems, spinodally decomposed alloys derive exceptional strength and corrosion resistance from their interpenetrating nanoscale phases, while block copolymer gyroids form porous electrodes that optimize transport in batteries (5–9).

A robust strategy for the fabrication of bicontinuous materials uses phase separation, a process in which a homogeneous fluid mixture spontaneously demixes into two distinct phases (10). The phase separation dynamics can generate a bicontinuous structure (11, 12). This structure, however, is inherently transient as the two phases coarsen over time reaching bulk phase separation (13, 14).

Thus, preserving bicontinuity requires kinetic arrest of the coarsening process. Established strategies include suppressing the fluidity of one of the two phases, either by replacing one of the two fluids with an elastomer network or by polymerizing one of the phase-separating fluids during coarsening (15–18). The interface itself can also be stabilized by adsorbing a high density of colloids on the interface to form mechanically stable “bijels” (19–21). Block copolymers offer an alternate method for generating bicontinuous structures through chemistry, but the scale of the resulting structure is controlled by the size of the constituent molecules (5–9). Here we describe a fundamentally different pathway for generating robust and tunable bicontinuous structures that uses active fluids and relies on mechanical, rather than chemical, control of soft interfaces.

Active fluids are composed of energy-consuming molecular units that collectively generate autonomous chaotic flows (22–26). Such flows and associated active stresses can power non-equilibrium dynamics and active assembly of passive colloids or fibers. They can also drive the deformation and actuation of soft interfaces and membranes (24, 27–38). We show how active flows continuously agitate the three-dimensional phase-separating mixture, transforming the conventional coarsening dy-

namics into a continuously reconfiguring bicontinuous network, which persists for the lifetime of the active fluid and is stable over a wide range of volume fractions. The bicontinuous structure is controlled by activity and surface tension. The interfacial curvature of active bicontinuous networks is dominated by sheet-like geometries, in contrast to passive phase-separating fluids dominated by minimal saddle-like surfaces (10, 39–42). The three-dimensional geometry studied here is qualitatively different from previous work which explored the role of microtubule-based activity on phase separation of PEO/dextran mixtures. One set of studies explored very thin chamber where the sample was effectively two dimensional (31, 33). Another study explored the effect of activity on the shape and stability of a bulk-separated interface in a three dimensional sample (32). Here, in contrast, we explore the morphology of the late stage phase separated state and demonstrate the stability of a remarkable bicontinuous structure.

2 Results

2.1 Theoretical model of active phase separation

We model an immiscible mixture of active and passive fluids in three-dimension within a continuum framework that couples Cahn-Hilliard phase separation to active nematodynamics. The concentration field $\phi(\mathbf{r})$ distinguishes the passive ($\phi = 0$) and the active ($\phi = 1$) phase, while the nematic tensor $\mathbf{Q}(\mathbf{r})$ captures the local orientational order within the active fluid. These fields are coupled through the incompressible Stokes flow $\mathbf{v}(\mathbf{r})$ and its spatial gradients (Methods 4.1) (32, 43, 44).

The phase separation between active and passive fluid is governed by the equilibrium surface tension γ . The sample composition is controlled by the active fraction $\phi_a = (1/V) \int d\mathbf{r} \phi(\mathbf{r})$, where $V = \int d\mathbf{r}$ is the total volume. The active stress tensor that drives Stokes flow is

$$\sigma^{\text{active}} = \alpha \phi \mathbf{Q}, \quad (1)$$

where $\alpha < 0$ is the extensile activity responsible for the turbulent-like dynamics of the active ($\phi = 1$) phase. We choose a parameter regime in which the nematic tensor $\mathbf{Q}(\mathbf{r})$ relaxes to the isotropic state ($\mathbf{Q} = 0$) in the absence of activity. Above a critical activity, active stresses destabilize the quiescent isotropic state and generate autonomous flows (45–48).

In passive systems, the well-mixed state is unstable over a range of parameters, leading to a spinodal instability with structures that coarsen over time. This reduces the interfacial energy, ultimately resulting in bulk phase separation (10, 13). Activity profoundly alters this process (49). At high activity, turbulent-like flows stir

the fluid and impede the thermodynamically driven phase separation (43, 50). Here we study intermediate activities that do not suppress phase separation, but arrest coarsening and influence the morphology of the phase separated state. In two dimensions, such moderate activity can generate percolating filamentary networks (44). These networks have a dynamical steady-state, with a characteristic length scale controlled by the balance of activity and surface tension.

2.2 Active phase separation

We study the behavior of the above-described theoretical model in three dimensions. Starting from an initial uniform well-mixed state, the mixture quickly reaches a phase separated structure with a characteristic length scale. The steady-state has a network-like morphology that percolates throughout the sample (Fig. 1B). The emerging labyrinthine structure consists of junction points that are connected by thread-like liquid bridges. The network is not static. The threads connecting different junctions appear to continuously rupture, while new ones are generated such microscopic dynamics generates a “living” continuously reconfiguring network-like structure.

To experimentally test these predictions, we combined a passive phase-separating polymer mixture of polyethylene oxide (PEO) and dextran with an active fluid (Materials and Methods) (31, 32, 51). The activity is generated by microtubules (MTs) and streptavidin-bound clusters of kinesin molecular motors (KSA) (Fig. 1F). Both protein-based components partition into the dextran-rich phase. The kinesin clusters bind to adjacent MTs, transforming the chemical energy from adenosine triphosphate (ATP) hydrolysis into interfilament sliding and bundle extension, which in turn drives large-scale turbulent flows.

Motivated by the theoretical prediction of bicontinuity we studied active phase separation in 100 μm thick chambers. The evolving structure was imaged with confocal microscopy. Internal activity generates large interfacial deformations that transform the morphology of the two coexisting phases, similar to what observed in simulations. Active flows generate a system spanning network-like structure (Fig. 1 C). The network is continuously reconfigured by the active flows (Movie. S2). Such dynamics persists for several hours, which is the active fluid lifetime (Fig. S4). In contrast, a passive system lacking active components forms minority-phase droplets that coarsen over time (Fig. S2).

2.3 Characterizing the bicontinuous morphology

Numerical simulations and experiments demonstrate that 3D active phase separation generates a steady-state dy-

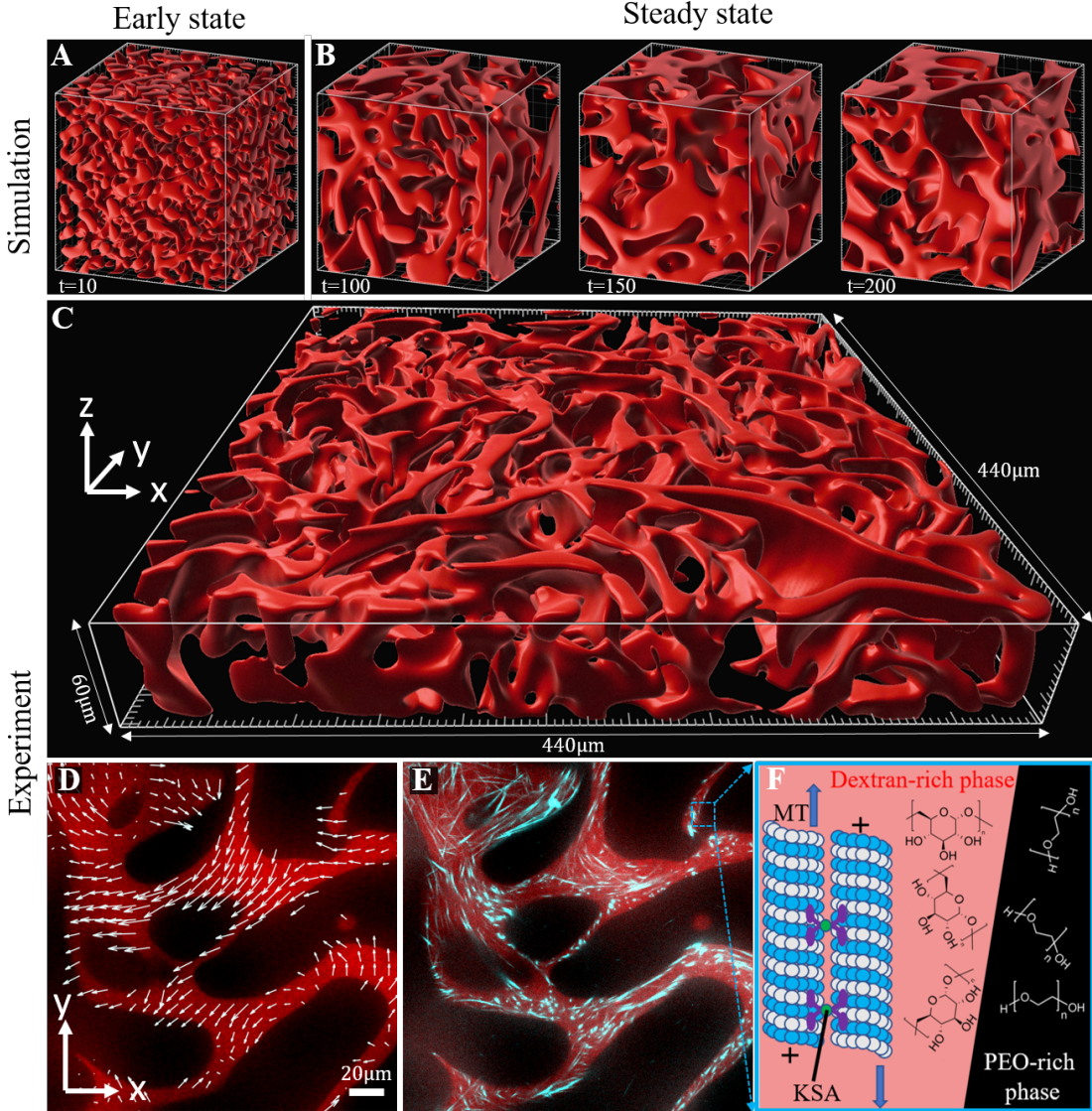


Figure 1: Active 3D phase separation yields a percolating network-like structure. (A-B) Evolution of the morphology of active phase separation in 3D computer simulations from the early state to the steady state. Red represents the active phase ($\phi > 0.5$). Simulation parameters: activity $|\alpha| = 1.30$, surface tension $\gamma = 1.0$, and active fraction $\phi_a = 0.40$. (C) Experimental morphology of the active phase (red) at steady state. The sample contains 92 nM KSA, 1.8% PEO, 1.8% dextran, and $\phi_a = 0.38$, imaged at time $t = 1.5$ h. (D) An x - y cross-section of a phase-separating sample. The white arrows indicate the active flows in the dextran phase (red), obtained from Particle Imaging Velocimetry. (E) MTs (cyan) partition into the dextran phase (red). (F) MTs in the dextran phase form bundles due to the depletion effect. Kinesin clusters (KSA) bind to MT bundles driving their extension.

namical structure. Both active and passive phases form distinct yet intercalated system-spanning networks. Taken together, they generate a bicontinuous structure (Fig. 2 A,C). To analyze the bicontinuity we threshold the 3D structure into passive and active regions, corresponding to $\phi < 0.5$ and $\phi > 0.5$, respectively. The connectedness

fraction, f_c , of each phase is defined as the volume of the largest connected active/passive component divided by the total volume of that component (44).

To determine the range of bicontinuity, we vary the fraction of the active phase ϕ_a , while keeping the activity and surface tension fixed. Bicontinuous structures, defined

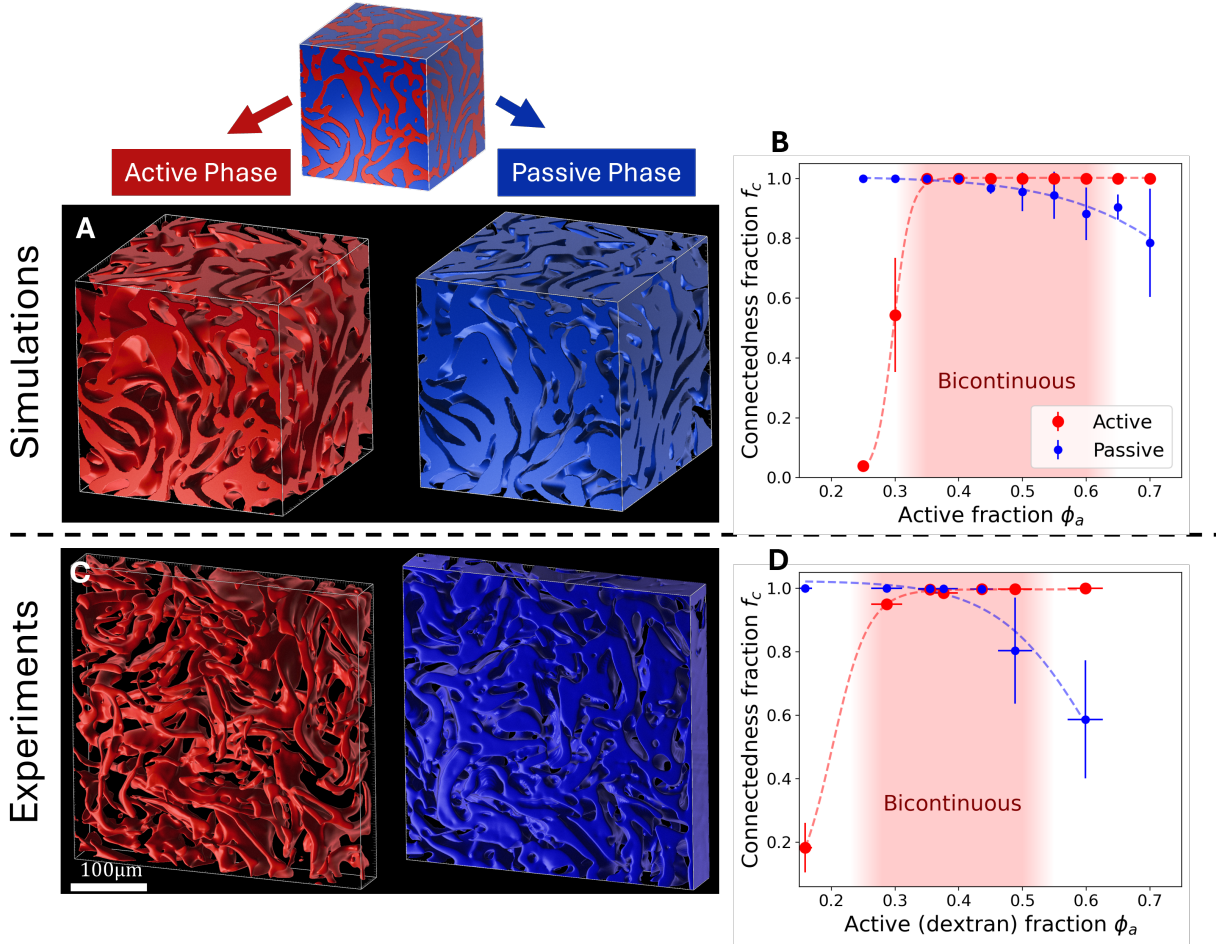


Figure 2: Bicontinuous morphology persists over a wide range of volume fractions. (A) Connected active (red) and passive phase (blue) in simulations, with $\phi_a = 0.40$ (B) Connectedness factor f_c of the active and passive phases as a function of the volume fraction of the active phase ϕ_a . The range where $f_c \approx 1$ for both phases highlighted in pink indicates bicontinuity. Simulation parameters: $|\alpha| = 0.70$, $\gamma = 1.0$. (C) Morphology of the connected active (red) and passive phase (blue) in the experiment. $\phi_a = 0.38$. (D) The connectedness fraction $f_c \approx 1$ for intermediate values of ϕ_a , indicating bicontinuity. Samples initially contain 183 nM KSA, 1.8% PEO, and 1.8% dextran.

as those where $f_c \approx 1$ for both phases, are observed from $0.3 < \phi_a < 0.6$ (Fig. 2 B). For $\phi_a < 0.3$, bicontinuity is broken as the active domains disintegrate into isolated droplets. For $\phi_a > 0.6$, the passive domains are broken up by active flows and become disconnected. The range of stable bicontinuous structures is controlled by activity and surface tension (Fig. S5). For example, doubling the activity generates stable bicontinuous structures over the entire regime of phase separation $0.0 < \phi_a < 1.0$.

Motivated by these predictions, we have explored the phase space of stable bicontinuous networks in experiments. We use a phase recombination method to keep the polymer concentration (surface tension) and the motor protein concentration (activity) fixed within each phase, while the active fraction ϕ_a varies between 0.16–0.60. We

(1) prepare an initial mixture with controlled concentrations of PEO, dextran and KSA, then (2) centrifuge the sample to generate bulk phase separation, and finally (3) recombine the two separated phases into a new mixture with chosen ϕ_a (Materials and Methods). The active (dextran) and passive (PEO) regions are differentiated using fluorescence intensity (Materials and Methods).

In experiments, the bicontinuous structure is observed over the range of volume fractions $0.3 < \phi_a < 0.5$ (Fig. 2D). For active fractions greater than 0.5, the passive phase disintegrates into droplets, while for fractions less than 0.3 the active phase breaks up into droplets, significantly decreasing f_c . Notably, the range of stable bicontinuous structures is not centered around $\phi_a = 0.5$: bicontinuity persists for a low volume fraction of the active

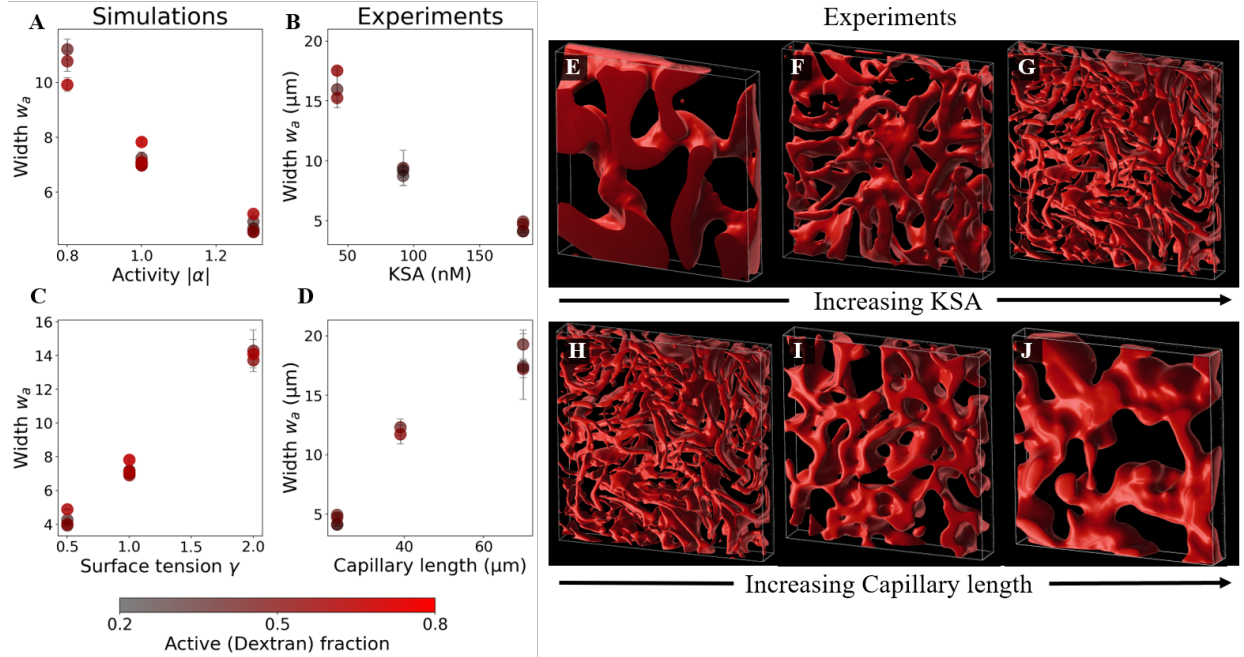


Figure 3: Active width w_a decreases with activity and increases with surface tension. (A-B) w_a decreases with activity $|\alpha|$ in simulations and with KSA concentration in experiments. (C-D) w_a increases with surface tension γ in simulations and with capillary length in experiments. In (A-D) the color of the dots represents the volume fraction ϕ_a of the active phase (see color bar) and shows that w_a is essentially independent of ϕ_a . (E-G) 3D visualization of the dextran phase (red) in experiments with increasing KSA concentration, showing a corresponding decrease of w_a . (H-J) 3D visualization of the dextran phase (red) in experiments with increasing capillary length, showing a corresponding increase of w_a . The experimental samples (B, E-G) contain initially 1.8% PEO and 1.8% dextran and varying KSA concentrations, 42 nM (E), 92 nM (F), and 183 nM (G). Samples (D, H-J) initially contain 183 nM KSA and varying PEO and dextran concentrations, both 1.8% (H), 1.9% (I), and 2.0% (J).

phase $\phi_a \approx 0.3$. In comparison, it disappears as soon as the active phase reaches the majority $\phi_a \approx 0.5$. This asymmetry suggests that the active phase containing MTs remains connected at a very low volume fraction, while the passive PEO-rich/MT-devout phase more easily breaks apart into the droplets. Intriguingly, similar asymmetry was observed in the directional invagination and break-up of a bulk three-dimensional active interface, where it was attributed to the nematic elasticity of the active fluid (32).

2.4 Controlling the morphology: active width

Simulations show that the morphology of the bicontinuous network is controlled by activity and surface tension. To characterize the structure, we measure the width w_a of the active network, defined as the surface to volume ratio of the largest connected active domain. We find that w_a increases with decreasing activity and with increasing equilibrium surface tension. Furthermore, w_a is essentially independent of the volume fraction ϕ_a (Fig. 3A,

C), suggesting that intrinsic dynamical active processes control the length scale of the bicontinuous morphology.

To experimentally test these predictions, we vary the KSA concentration, which is a proxy for activity, and the PEO/dextran concentration, which controls the surface tension. Due to a density difference, the dextran phase gradually sediments due to gravity over tens of minutes, causing a variation in w_a (Fig. S3). To minimize this effect, we continuously invert the top and bottom of the chamber by slowly rotating the samples. The sample is then moved from the rotation stage and imaged for a maximum duration of 5 minutes (Materials and Methods). The effective surface tension is estimated from measurements of the capillary length for different PEO/dextran concentrations (Fig. S1). The experimental trends follow the predictions of the numerical model: increasing surface tension increases w_a ; increasing activity decreases w_a (Fig. 3 A-D). Furthermore, w_a is largely independent of the volume fraction.

The behavior of the width w_a suggests that the morphology is controlled by two competing mechanisms: the

stretching of the interface due to extensile active flows and its relaxation controlled by surface tension. Extensile active forces are known to align the nematic director with the interface (32, 52, 53). This alignment then drives active shear flows that tangentially stretch the interface. The stretching is countered by surface tension that tends to shorten the interface. In general we expect activity to also modify the surface tension, as shown for instance in scalar models of active phase separation (49). Here we assume that the main effect of activity is to build up local nematic order and align the liquid crystal with the interface, and use the bare (passive) surface tension in the scaling arguments below. In the isotropic liquid crystalline phase, the active stretching rate can be approximated as

$$\tau_{\text{active}}^{-1} \sim \frac{S(|\alpha| - \alpha_c)}{\eta} \sim \frac{(|\alpha| - \alpha_c)^{3/2}}{\eta}, \quad (2)$$

where η is the fluid viscosity, S is the scalar nematic order parameter and α_c is the threshold above which activity drives local nematic order (32, 44) (see Methods Section). We approximate the scalar order parameter with the mean value generated by activity, $S \sim \sqrt{(|\alpha| - \alpha_c)}$ (47, 54). In three-dimensions, the rate at which the interface relaxes due to surface tension is given by

$$\tau_{\text{diffusive}}^{-1} \sim \frac{\gamma}{V}, \quad (3)$$

where V is the total volume of the active domain. We write this as $V = w_a^{d_f} \ell^{(3-d_f)}$, where w_a is the width of the active region, ℓ is set by mass conservation, and $d_f < 3$ is controlled by the active process (44). Tube-like filamentary structures correspond to $d_f = 2$ whereas sheet-like structures, with one short axis, correspond to $d_f = 1$. At steady state, the active width is determined by balancing active stretching and interfacial relaxation, $\tau_{\text{active}}^{-1} \sim \tau_{\text{diffusive}}^{-1}$, with the result

$$w_a \sim \left(\frac{\gamma}{(|\alpha| - \alpha_c)^{3/2}} \right)^{1/d_f} = \left(\frac{|\alpha| - \alpha_c}{\gamma^{2/3}} \right)^{-3/2d_f}. \quad (4)$$

Using simulations, we have measured the active width as a function of both activity and surface tension. The collapse of the data supports a scaling law $w_a \sim ((|\alpha| - \alpha_c)/\gamma^{2/3})^\nu$, with $\nu \approx -1.36$, corresponding to $d_f = -3/(2\nu) \approx 1.1$ (Fig. 4). This scaling suggests that the bicontinuous morphology is dominated by sheet-like active domains, whose width is governed by the balance of active stretching and passive relaxation.

2.5 Characterizing curvature and morphology

The scaling argument described above suggests the dominance of sheet-like structures. Motivated by this

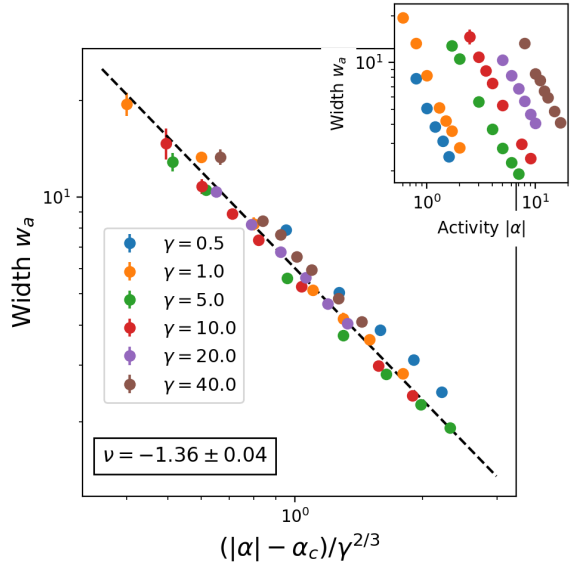


Figure 4: Steady state width w_a = Volume/Surface Area of the connected active domain in the bicontinuous region as a function of activity $|\alpha|$ and equilibrium surface tension γ , for a fixed active fraction $\phi_a = 0.40$. The main figure shows that the data collapse when plotted versus $(|\alpha| - \alpha_c)/\gamma^{2/3}$ (Eq. 4). The black dashed line shows the best fit (via linear regression) to $w_a \sim ((|\alpha| - \alpha_c)/\gamma^{2/3})^\nu$ for $\nu = -1.36 \pm 0.04$. The inset shows the unscaled active width as a function of activity, for various values of γ . Fixed parameters: $K = 24.0$, $\alpha_c = 2\eta r/\lambda\Gamma = 0.2$.

prediction, we measured the surface curvature of the active/passive interfaces. We compute the values of the two principal curvatures $\kappa_1(\mathbf{s})$ and $\kappa_2(\mathbf{s})$, where \mathbf{s} is a point on the interface \mathcal{S} . We choose $\kappa_1 < \kappa_2$, everywhere on the phase-separated interface (Fig. 5A) (Materials and Methods). We show representative visualizations of the normalized Gaussian curvature $w_a^2 \kappa_1(\mathbf{s}) \kappa_2(\mathbf{s})$ for $\mathbf{s} \in \mathcal{S}$, where w_a is to the width of the active phase, as defined in the previous section. In both experiments and simulations, the surface generated by active phase separation is dominated by regions of normalized Gaussian curvature close to zero (Fig. 5 B,C). We contrast this with the transient morphology obtained in passive phase separation from the Cahn-Hilliard equation, which is dominated by saddle-like surfaces with negative Gaussian curvature (10, 39–42) (Fig. 5D).

From the principal curvature values, we compute the joint probability distributions $\rho(\kappa_1, \kappa_2)$. Different regions in the κ_1 - κ_2 plane indicate different surfaces (Fig. 5E). In both experiments and simulations, the joint distribution is peaked at small values of both κ_1 and κ_2 , which corresponds to sheet-like domains (Fig. 5F, G). The vertical and horizontal branches centered around zero-

curvature corresponds to cylinder-like surfaces, which are associated with the sheet edges. In comparison, the probability distribution obtained from the Cahn-Hilliard equation is characterized by large positive-negative pairs of principal curvatures correspond to saddle-like surfaces (Fig. 5H). The curvature analysis supports the finding that the connected active domain is dominated by sheet-like structures.

3 Discussion

Activity transforms the coarsening domains of passive three-dimensional phase separation into a steady state bicontinuous structure that continuously reconfigures in time, while maintaining its morphology. The bicontinuous morphology is observed in a dynamical steady-state across a wide range of volume fractions, while its width is controlled by activity and surface tension. Active bicontinuous structure is composed of sheet-like domains, in contrast to saddle-like interfaces observed in passive phase separation (10, 39–42).

There is a stark contrast between how bicontinuous structures form in passive and active fluids (12, 55). In both cases, passive restorative forces such as interfacial tension drive the system to a state of minimal surface area. In a passive system, established strategies to preserve bicontinuity in steady state therefore either engineer the system's chemistry, like tailoring molecular interactions in block copolymers, or kinetically arrest the structure by solidifying one phase or the interface itself (5–9, 15–21). In contrast, active fluid maintains a dynamical, bicontinuous steady state over its entire lifetime, which is determined by the available chemical fuel.

The effect of activity on phase separation has been explored both experimentally and theoretically. In particular, extensive theoretical work has been carried out in scalar models of active/passive mixtures, where the mixture is described entirely in terms of the conserved concentration field, coupled to flow (49, 56, 57). In this limit, active stresses are driven by gradients of the concentration field and are therefore localized at the interface. These models exhibit arrested coarsening driven by the competition between active stress and interfacial tension. In a different limit studied here, isotropic or nematic liquid crystal and their associated active stresses are present throughout the bulk of the active fluid (31–33, 37, 58, 59). An important interaction for the formation of bicontinuous structures is active anchoring at the interface (52), where the active units align along the interfaces to generate autonomous flows that stretch the active phase into sheet-like domains (Fig. 5). This elongation continuously connects separate droplets into a network and dynamically balances the collapsing effect of surface tension. Whether bicontinuous

structures can be obtained in three-dimensional scalar models, perhaps as a result of active renormalization of surface tension, remains, to our knowledge, an open question.

The structures in active phase separation are determined by the competition between active stress and surface tension. We have shown that this competition controls the width of the active sheets (Fig. 4). Extreme values of activity, however, break bicontinuity resulting in distinct behaviors. On the one hand, when activity is very small compared to surface tension, active flows cannot significantly elongate the droplets, but only induce small interfacial deformations. In this case, one of the two phases irreversibly turns into droplets through a Plateau-Rayleigh instability (13, 37). On the other hand, when activity is very high, the associated energy input is large enough to overcome the effect of the thermodynamic chemical potential, suppressing the phase separation itself and generating a uniform mixture (43, 50).

Biological and biomimetic systems are known for their flexibility and the capability to self-heal. This stems from their use of continuous energy input, which allows them to maintain dynamical steady states, adapt to damage, and resist degenerative processes such as coarsening. Our work demonstrates how this principle can be applied to synthetic systems to generate controllable structures not achievable in equilibrium.

4 Materials and Methods

4.1 Continuum model and simulation details

We use a continuum model of phase separation in a mixture of an active liquid crystal and passive fluid. The model couples Cahn-Hilliard dynamics to the hydrodynamic of a nematic liquid crystal. It is formulated in terms of coupled equations for the phase fraction ϕ of active fluid, the nematic order parameter \mathbf{Q} and fluid flow \mathbf{v} , given by

$$\begin{aligned} \partial_t \phi + \mathbf{v} \cdot \nabla \phi &= M \nabla^2 \mu, \\ \partial_t \mathbf{Q} + \mathbf{v} \cdot \nabla \mathbf{Q} + [\Omega, \mathbf{Q}] &= \lambda \mathbf{A} + \frac{1}{\Gamma} \mathbf{H}, \\ 0 &= \eta \nabla^2 \mathbf{v} - \nabla P + \nabla \cdot \boldsymbol{\sigma}, \end{aligned} \quad (5)$$

where $\phi(\mathbf{r}) \in [0, 1]$. The Stokes flow $\mathbf{v}(\mathbf{r})$ and its gradients given by the strain rate $A_{ij} = (\partial_i v_j + \partial_j v_i)/2$ and the vorticity tensor $\Omega_{ij} = (\partial_i v_j - \partial_j v_i)/2$ couple ϕ and \mathbf{Q} .

Phase separation between the active ($\phi = 1$) and the passive fluid ($\phi = 0$) is driven by the chemical potential $\mu = \delta F_\phi / \delta \phi$, where $F_\phi = (3\gamma/\xi) \int d\mathbf{r} \phi^2 (\phi - 1)^2 + \xi^2 (\nabla \phi)^2 / 2$. Here γ is the equilibrium surface tension and ξ is the width of the equilibrium interface between the two phases. We characterize the composition of the

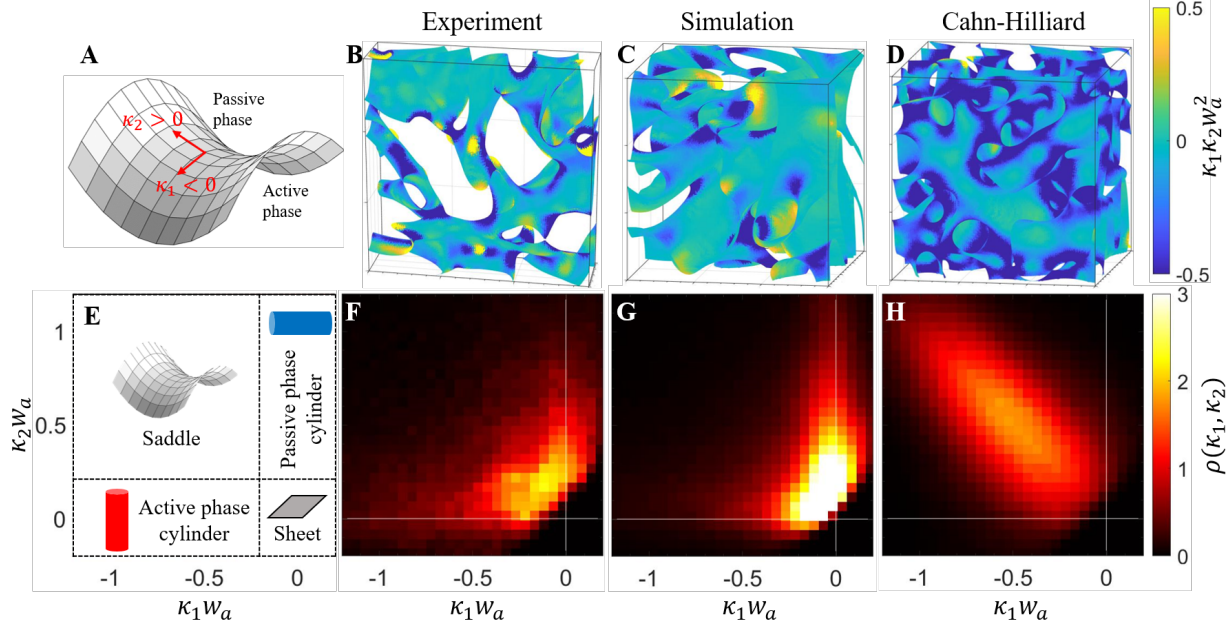


Figure 5: Comparing the interface morphology in passive and active bicontinuous structures. (A) The two principal curvatures κ_1 and κ_2 are calculated everywhere on the interface. (B-D) 3D visualization of the normalized Gaussian curvature $\kappa_1\kappa_2w_a^2$ of the interface from experiment (B), simulations of the active/passive mixture(C) and simulations of the passive Cahn-Hilliard equation (D). The color indicates the value of the Gaussian curvature. (E-H) Distribution $\rho(\kappa_1, \kappa_2)$ of normalized principal curvatures κ_1w_a and κ_2w_a . Different values of κ_1 and κ_2 correspond to different geometries (E). ρ peaks at small values of κ_1 and κ_2 in experiments (F) and simulations (G), indicating sheet-like interfaces. ρ peaks at $\kappa_1 \ll 0, \kappa_2 \gg 0$ in simulations of the Cahn-Hilliard equation (H), indicating a saddle-like interface. The experimental sample (B,F) contains 92 nM KSA, 1.8% PEO, 1.8% dextran, and $\phi_a = 0.38$. Simulation parameters (C,G): $|\alpha| = 1.30$, $\gamma = 1.0$, and $\phi_a = 0.40$.

fluid mixture using the (conserved) active fraction $\phi_a = \int d\mathbf{r} \phi(\mathbf{r})$.

The (traceless) nematic tensor \mathbf{Q} captures the local nematic orientational order inside the active fluid. The molecular field $H_{ij} = (\delta F_Q / \delta Q_{ij})^{S,T}$ controls the relaxation of the nematic tensor via the Landau-de Gennes free energy $F_Q = \int d\mathbf{r} r \text{Tr}\{\mathbf{Q}^2\}/2 + w \text{Tr}\{\mathbf{Q}^3\}/3 + u \text{Tr}\{\mathbf{Q}^2\}^2/4 + K(\nabla \mathbf{Q})^2/2$, with $r, u > 0$.

The nematic field is defined everywhere, but in the absence of activity it relaxes to $\mathbf{Q} = 0$ since $r > 0$. Due to the flow alignment and vorticity couplings, self-generated flows result in non-zero local nematic order within the active ($\phi = 1$) phase, as we discuss below.

The flow is governed by the Stokes equation with incompressibility, i.e., $\nabla \cdot \mathbf{v} = 0$ enforced via the pressure P . The stress tensor ($\sigma = \sigma^c + \sigma^a$) consists of the capillary stress ($\nabla \cdot \sigma^c = -\phi \nabla \mu$), and the active stress, σ^a , proportional to the phase field ϕ and the local nematic order Q_{ij} i.e.

$$\sigma^a = \alpha \phi \mathbf{Q}, \quad (6)$$

with $\alpha < 0$ corresponding to extensile activity. Within the active phase ($\phi = 1$) self generated flows arise above a critical activity $\alpha_c = 2\eta r/\lambda\Gamma$. For $|\alpha| > \alpha_c$, the positive feedback of flow alignment due to the active flows generated by perturbations of the nematic field leads to active turbulence (45–48).

Unless otherwise specified, the parameter values are reported in time units of Γ/u , length units of $\sqrt{M\Gamma}$ and energy density in units of u . Throughout this paper, we fix the flow alignment parameter $\lambda = 1.0$, viscosity $\eta = 1.0$, interface width $\xi = \sqrt{3/2}$ and free energy parameters $r = 0.1$, $w = 0$.¹ We consider different values of the nematic elasticity K , and systematically vary the activity $|\alpha|$, the equilibrium surface tension γ , and the active volume fraction ϕ_a . The simulations are done with periodic boundary conditions and performed using self-developed pseudo spectral solvers (60) on a uniform three-

¹We only consider large nematic order generated by active stresses, away from the isotropic to nematic transition, and hence can safely ignore the cubic term that appears in 3D. We verify in simulations that including a non-zero cubic energy contribution does not affect the stability of the bicontinuous phase.

dimensional grid of size $170 \times 170 \times 170$, typically for 10^5 - 10^6 time steps until at least the system reaches steady state.

4.2 Experimental Design

The phase separation system and the MT-based active system were based on previous protocols (31, 32), with a decreased concentration of coexisting polymers to reduce surface tension. PEO (100 kDa, Sigma-Aldrich) and dextran (450 to 650 kDa, Sigma-Aldrich) were added into M2B buffer (80 mM K-pipes, 2 mM MgCl₂, 1 mM EGTA, pH 6.8). We varied their initial concentrations to three values during our experiment: 1.8% PEO and 1.8% dextran, 1.9% PEO and 1.9% dextran and 2.0% PEO and 2.0% dextran, which controlled the capillary length of the sample (Fig. S1). For visualization, we added a very small amount (<0.1% w/w) of amino-dextran (Fina Biosolutions) fluorescently labeled with Alexa-Fluor 488 NHS Ester (Invitrogen).

Tubulin was purified and labeled as described in previous work (61). A minor tubulin fraction (3%) was conjugated to AZDye 647 NHS Ester (Fluoroprobe) using a succinimidyl ester linkage. Labeled and unlabeled tubulin monomers were co-polymerized into microtubules (MTs) at 37 °C using 0.6 mM guanylyl-(alpha,beta)-methylene-diphosphonate (GMPCPP, Gena Biosciences) and 1.2 mM Dithiothreitol (DTT, Gena Biosciences) in M2B buffer (61). The MTs were sonicated for 60 seconds in a Branson 1800 sonicator to reduce the bundle rigidity. The final concentration of MTs was 0.67 mg/mL. Kinesin-401 protein fused to a biotin-carboxyl carrier domain was expressed and purified using established protocols (61). This protein was subsequently combined with tetrameric streptavidin in an M2B buffer with 5 mM DTT, forming a kinesin-streptavidin cluster (KSA). The final concentrations of KSA in the samples varied from 42-183 nM.

The PEO-dextran mixture was mixed together with MTs, KSA, caged ATP (NPE-caged adenosine triphosphate, P3-(1-(2-nitrophenyl)ethyl) ester, disodium salt, 1 mM final), antioxidants, and an ATP regeneration system made according to established protocols (61). The antioxidants contained (in final concentrations) 2 mM Trolox, 5 mM DTT, 3.3 mg/mL glucose, 200 µg/mL glucose oxidase, and 35 µg/mL catalase dissolved in a phosphate buffer (20 mM K₂HPO₄ and 100 mM KCl in DI water, pH 7.4). The ATP regeneration system contained (in final concentrations) 26 mM phosphoenol Pyruvate (PEP) (Beantown Chemical) and pyruvate kinase/lactate dehydrogenase (Sigma-Aldrich) dissolved in M2B.

During each experiment, a large 48 µL mixture containing the ingredients above was first made in an Eppendorf tube. The sample was then centrifuged at 2000 g relative

centrifugal force for 1 min (Fisher Scientific, 05090-128) to bulk separate the PEO-rich and dextran-rich phases, with the PEO phase on the top, dextran phase at the bottom, and a clear flat interface in between. At this step, MTs and KSA partitioned into the dextran phase. The two separated phases were then pipetted out separately into two containers. We pipetted out small amounts from these two separated containers and mixed into a new 8 µL small sample. The fraction of the dextran phase in this 8 µL sample is the active fraction ϕ_a . This remixing procedure ensured the concentration of all components within each phase remained the same across these samples while ϕ_a was varied between 0.15-0.60 (Fig. 2, Fig. 3). The whole procedure was performed in a dark room to avoid releasing the caged ATP and activating the sample.

The final active sample was vortex-mixed for 10s (Genie-2 Vortex Mixer) and placed within the chamber constructed by flanking the parafilm with two Polyethylene glycol (PEG) coated glass coverslips. The coverslips were coated by applying 10% (w/w) mPEG-silane (20 kDa, Biopharma) dissolved in anhydrous Dimethyl sulfoxide (DMSO) (62). The constructed chamber had a dimension of 4mm×18mm×0.1mm. The chamber was sealed with adhesive glue (Norland) and the glue was polymerized through 30-second exposure to ultraviolet light. This UV exposure unleashed the caged ATP at the same time and made the sample active.

The samples were imaged with epifluorescence microscopy, with a spinning disk confocal microscope (X-Light V2, CrestOptics) and a sCMOS camera (Prime95B, Photometrics) and binned to obtain 804×804 squared pixels. Samples with initially 2.0% PEO, 2.0% dextran and samples with 42 nM KSA were imaged using a 10x air immersion objective (NA=0.5) with a 2 µm z-step. Other samples were imaged with a 40x water immersion objective (NA=1.15) with a 1 µm z-step. Samples with initially 1.8% PEO, 1.8% dextran and 183 nM KSA were imaged in dextran and MT channels and had a 14 s time interval. Other samples were imaged only in the dextran channel and had a 7 s time interval.

The dextran phase had a slightly larger density than the PEO phase, causing a sedimentation in the $-z$ direction due to gravity over tens of minutes. This would finally lead to two bulk phase separated phases, with the active phase perforated with passive droplets at the bottom of the chamber. To minimize this effect, after the samples were activated, they were placed on a rotator (Benchmark Scientific H2020 Roto-Therm) and rotated at 24 rpm at room temperature for 1.5 hours. This ensured that the samples were in steady state without sedimentation (Fig. S4). The samples were then immediately transferred to the microscope and imaged consecutively for 5 minutes (Fig. S3).

4.3 Data Analysis

The experimental data were analyzed using established methods (32). Confocal microscopy images were first classified into the dextran-rich phase and PEO-rich phase with the machine-learning software Ilastik based on intensity thresholding (63). The interface was extracted between the two phases to calculate the width of the structure (Fig. 3). The interface was then transformed into a triangular mesh form using the software MeshLab (64). The curvature was then calculated using published codes in MATLAB (65, 66). 3D visualization of both simulation and experiment data was done with software Imaris (Fig. 1,2,3) (67).

References and Notes

1. D. Holcman, *et al.*, Single particle trajectories reveal active endoplasmic reticulum luminal flow. *Nature cell biology* **20** (10), 1118–1125 (2018).
2. M. J. Dayel, E. F. Hom, A. S. Verkman, Diffusion of green fluorescent protein in the aqueous-phase lumen of endoplasmic reticulum. *Biophysical journal* **76** (5), 2843–2851 (1999).
3. X. S. Liu, P. Sajda, P. K. Saha, F. W. Wehrli, X. E. Guo, Quantification of the roles of trabecular microarchitecture and trabecular type in determining the elastic modulus of human trabecular bone. *Journal of Bone and Mineral Research* **21** (10), 1608–1617 (2006).
4. F. Herisson, *et al.*, Direct vascular channels connect skull bone marrow and the brain surface enabling myeloid cell migration. *Nature neuroscience* **21** (9), 1209–1217 (2018).
5. C. Wu, G. Thomas, Microstructure and properties of a Cu-Ni-Cr spinodal alloy. *Metallurgical Transactions A* **8** (12), 1911–1916 (1977).
6. E. L. Thomas, *et al.*, Ordered bicontinuous double-diamond structure of star block copolymers: a new equilibrium microdomain morphology. *Macromolecules* **19** (8), 2197–2202 (1986).
7. S. Shi, Y. Li, B.-N. Ngo-Dinh, J. Markmann, J. Weissmüller, Scaling behavior of stiffness and strength of hierarchical network nanomaterials. *Science* **371** (6533), 1026–1033 (2021).
8. J. Werner, G. Rodríguez-Calero, H. Abruña, U. Wiesner, Block copolymer derived 3-D interpenetrating multifunctional gyroidal nanohybrids for electrical energy storage. *Energy & Environmental Science* **11** (5), 1261–1270 (2018).
9. J. Han, *et al.*, Role of bicontinuous structure in elastomeric electrolytes for high-energy solid-state lithium-metal batteries. *Advanced Materials* **35** (1), 2205194 (2023).
10. J. W. Cahn, J. E. Hilliard, Free energy of a nonuniform system. I. Interfacial free energy. *The Journal of chemical physics* **28** (2), 258–267 (1958).
11. N. Lorén, M. Langton, A.-M. Hermansson, Determination of temperature dependent structure evolution by fast-Fourier transform at late stage spinodal decomposition in bicontinuous biopolymer mixtures. *The Journal of chemical physics* **116** (23), 10536–10546 (2002).
12. H. Jinnai, H. Watashiba, T. Kajihara, M. Takahashi, Connectivity and topology of a phase-separating bicontinuous structure in a polymer mixture: Direct measurements of coordination number, inter-junction distances and Euler characteristic. *The Journal of chemical physics* **119** (14), 7554–7559 (2003).
13. E. D. Siggia, Late stages of spinodal decomposition in binary mixtures. *Physical review A* **20** (2), 595 (1979).
14. A. J. Bray, Theory of phase-ordering kinetics. *Advances in Physics* **51** (2), 481–587 (2002).
15. C. Fernández-Rico, *et al.*, Elastic microphase separation produces robust bicontinuous materials. *Nature Materials* **23** (1), 124–130 (2024).
16. P. K. Chan, A. D. Rey, Polymerization-induced phase separation. 1. Droplet size selection mechanism. *Macromolecules* **29** (27), 8934–8941 (1996).
17. M. J. Lee, *et al.*, Elastomeric electrolytes for high-energy solid-state lithium batteries. *Nature* **601** (7892), 217–222 (2022).
18. M. Z. Müller, *et al.*, Cell-guiding microporous hydrogels by photopolymerization-induced phase separation. *Nature Communications* **16** (1), 4923 (2025).
19. K. Stratford, R. Adhikari, I. Pagonabarraga, J.-C. Desplat, M. E. Cates, Colloidal jamming at interfaces: A route to fluid-bicontinuous gels. *Science* **309** (5744), 2198–2201 (2005).
20. E. M. Herzig, K. White, A. B. Schofield, W. C. Poon, P. S. Clegg, Bicontinuous emulsions stabilized solely by colloidal particles. *Nature materials* **6** (12), 966–971 (2007).
21. C. Huang, *et al.*, Bicontinuous structured liquids with sub-micrometre domains using nanoparticle surfactants. *Nature nanotechnology* **12** (11), 1060–1063 (2017).
22. R. Aditi Simha, S. Ramaswamy, Hydrodynamic fluctuations and instabilities in ordered suspensions of self-propelled particles. *Physical review letters* **89** (5), 058101 (2002).
23. D. Saintillan, M. J. Shelley, Instabilities and Pattern Formation in Active Particle Suspensions: Kinetic Theory and Continuum Simulations. *Physical Review Letters* **100** (17), 178103 (2008).
24. T. Sanchez, D. T. Chen, S. J. DeCamp, M. Heymann, Z. Dogic, Spontaneous motion in hierarchically assembled active matter. *Nature* **491** (7424), 431–434 (2012).

25. H. H. Wensink, *et al.*, Meso-scale turbulence in living fluids. *Proceedings of the national academy of sciences* **109** (36), 14308–14313 (2012).

26. S. Zhou, A. Sokolov, O. D. Lavrentovich, I. S. Aranson, Living liquid crystals. *Biophysical Journal* **106** (2), 420a (2014).

27. X.-L. Wu, A. Libchaber, Particle diffusion in a quasi-two-dimensional bacterial bath. *Physical review letters* **84** (13), 3017 (2000).

28. J. Berezney, *et al.*, Controlling assembly and oscillations of elastic membranes with an active fluid. *arXiv preprint arXiv:2408.14699* (2024).

29. Q. Martinet, Y. Li, A. Aubret, E. Hannezo, J. Palacci, Emergent dynamics of active elastic microbeams. *Physical Review X* **15** (4), 041017 (2025).

30. D. Grober, *et al.*, Unconventional colloidal aggregation in chiral bacterial baths. *Nature Physics* **19** (11), 1680–1688 (2023).

31. R. Adkins, *et al.*, Dynamics of active liquid interfaces. *Science* **377** (6607), 768–772 (2022).

32. L. Zhao, *et al.*, Asymmetric fluctuations and self-folding of active interfaces. *Proceedings of the National Academy of Sciences* **121** (51), e2410345121 (2024).

33. B. C. Sessa, F. Cao, R. A. Pelcovits, T. R. Powers, G. Duclos, Interfacial instability of confined 3D active droplets (2025), <https://arxiv.org/abs/2506.17532>.

34. S. C. Takatori, A. Sahu, Active contact forces drive nonequilibrium fluctuations in membrane vesicles. *Physical review letters* **124** (15), 158102 (2020).

35. A. Sciortino, *et al.*, Active membrane deformations of a minimal synthetic cell. *Nature Physics* pp. 1–9 (2025).

36. F. C. Keber, *et al.*, Topology and dynamics of active nematic vesicles. *Science* **345** (6201), 1135–1139 (2014).

37. J. Laprade, *et al.*, Coarsening of biomimetic condensates in a self-stirring active fluid. *arXiv preprint arXiv:2509.21753* (2025).

38. C. Liu, D. Cao, S. Liu, Y. Wu, Nonequilibrium dynamics of membraneless active droplets. *arXiv preprint arXiv:2511.04181* (2025).

39. T. Araki, H. Tanaka, Three-dimensional numerical simulations of viscoelastic phase separation: Morphological characteristics. *Macromolecules* **34** (6), 1953–1963 (2001).

40. D. A. Beysens, Kinetics and morphology of phase separation in fluids: The role of droplet coalescence. *Physica A: Statistical Mechanics and its Applications* **239** (1-3), 329–339 (1997).

41. Y. Kwon, K. Thornton, P. W. Voorhees, Coarsening of bicontinuous structures via nonconserved and conserved dynamics. *Physical Review E* **75** (2), 021120 (2007).

42. F. Perrot, *et al.*, Morphology transition observed in a phase separating fluid. *Physical Review E* **59** (3), 3079 (1999).

43. F. Caballero, M. C. Marchetti, Activity-suppressed phase separation. *Physical Review Letters* **129** (26), 268002 (2022).

44. P. Gulati, F. Caballero, M. Cristina Marchetti, Active fluids form system-spanning filamentary networks. *Physical Review Letters* **134** (13), 138301 (2025).

45. E. Putzig, G. S. Redner, A. Baskaran, A. Baskaran, Instabilities, defects, and defect ordering in an over-damped active nematic. *Soft matter* **12** (17), 3854–3859 (2016).

46. P. Srivastava, P. Mishra, M. C. Marchetti, Negative stiffness and modulated states in active nematics. *Soft matter* **12** (39), 8214–8225 (2016).

47. S. Santhosh, M. R. Nejad, A. Doostmohammadi, J. M. Yeomans, S. P. Thampi, Activity induced nematic order in isotropic liquid crystals. *Journal of Statistical Physics* **180** (1), 699–709 (2020).

48. F. Vafa, M. J. Bowick, B. I. Shraiman, M. C. Marchetti, Fluctuations can induce local nematic order and extensile stress in monolayers of motile cells. *Soft Matter* **17** (11), 3068–3073 (2021).

49. M. E. Cates, C. Nardini, Active phase separation: new phenomenology from non-equilibrium physics. *Reports on Progress in Physics* **88** (5), 056601 (2025).

50. A. M. Tayar, *et al.*, Controlling liquid–liquid phase behaviour with an active fluid. *Nature Materials* **22** (11), 1401–1408 (2023).

51. Y. Liu, R. Lipowsky, R. Dimova, Concentration dependence of the interfacial tension for aqueous two-phase polymer solutions of dextran and polyethylene glycol. *Langmuir* **28** (8), 3831–3839 (2012).

52. M. L. Blow, S. P. Thampi, J. M. Yeomans, Biphasic, lyotropic, active nematics. *Physical review letters* **113** (24), 248303 (2014).

53. R. C. Coelho, H. R. Figueiredo, M. M. Telo da Gama, Active nematics on flat surfaces: from droplet motility and scission to active wetting. *Physical Review Research* **5** (3), 033165 (2023).

54. L. Giomi, L. Mahadevan, B. Chakraborty, M. Hagan, Banding, excitability and chaos in active nematic suspensions. *Nonlinearity* **25** (8), 2245 (2012).

55. E. Scholten, L. M. Sagis, E. van der Linden, Coarsening rates of bicontinuous structures in polymer mixtures. *Macromolecules* **38** (8), 3515–3518 (2005).

56. A. Tiribocchi, R. Wittkowski, D. Marenduzzo, M. E. Cates, Active model H: scalar active matter in a momentum-conserving fluid. *arXiv preprint arXiv:1504.07447* (2015).

57. R. Singh, M. Cates, Hydrodynamically interrupted droplet growth in scalar active matter. *arXiv preprint arXiv:1907.04819* (2019).

58. P. Gulati, F. Caballero, I. Kolvin, Z. You, M. C. Marchetti, Traveling waves at the surface of active liquid crystals. *Soft Matter* **20** (38), 7703–7714 (2024).

59. F. Kempf, R. Mueller, E. Frey, J. M. Yeomans, A. Doostmohammadi, Active matter invasion. *Soft matter* **15** (38), 7538–7546 (2019).

60. F. Caballero, cuPSS: a package for pseudo-spectral integration of stochastic PDEs. *Benchmarking* **11**, 14 (2024).

61. A. M. Tayar, L. M. Lemma, Z. Dogic, Assembling microtubule-based active matter, in *Microtubules: Methods and Protocols* (Springer), pp. 151–183 (2022).

62. Y. Gidi, S. Bayram, C. J. Ablenas, A. S. Blum, G. Cosa, Efficient one-step PEG-silane passivation of glass surfaces for single-molecule fluorescence studies. *ACS applied materials & interfaces* **10** (46), 39505–39511 (2018).

63. S. Berg, *et al.*, Ilastik: interactive machine learning for (bio) image analysis. *Nature methods* **16** (12), 1226–1232 (2019).

64. P. Cignoni, *et al.*, Meshlab: an open-source mesh processing tool., in *Eurographics Italian chapter conference* (Salerno), vol. 2008 (2008), pp. 129–136.

65. N. P. Mitchell, D. Cislo, gut_matlab. GitHub repository (2025), https://github.com/npmitchell/gut_matlab (accessed on 6/6/2025).

66. S. Rusinkiewicz, Estimating curvatures and their derivatives on triangle meshes, in *Proceedings. 2nd International Symposium on 3D Data Processing, Visualization and Transmission, 2004. 3DPVT 2004.* (IEEE) (2004), pp. 486–493.

67. Oxford Instruments, Imaris (2024), <https://imaris.oxinst.com>.

Funding: This work was primarily supported by the US Department of Energy, Office of Basic Energy Sciences under award number DE-SC0019733. Development and optimization of the two-phase system of active liquid–liquid phase separation was supported by NSF-ISS-2224350. OS and MT acknowledge support of NSF-MRSEC DMR 2308708. We also acknowledge the use of the biosynthesis facility supported by NSF-MRSEC-2011846 and NRI-MCDB Microscopy Facility supported by the NIH Shared Instrumentation Grant 1S10OD019969-01A1. Use was made of computational facilities purchased with funds from the NSF(CNS-1725797) and administered by the Center for Scientific Computing (CSC). The CSC is supported by the California NanoSystems Institute and the Materials Research Science and Engineering Center (NSF DMR 2308708).

Author contributions: P.G., L.Z., Z.D., and M.C.M designed research; P.G., and L.Z. performed research; P.G., L.Z., and M.T. analyzed data; P.G., L.Z., M.T., O.A.S., Z.D., and M.C.M. wrote the paper.

Competing interests: The authors declare that they have no competing interests.

Supplementary materials

- Materials and Methods
- Supplementary Text
- Figs. S1 to S3
- Tables S1 to S4
- References (7-67)
- Movie S1
- Data S1

Supplementary Materials for Dynamical bicontinuous networks from 3D active phase separation

Paarth Gulati^{1†}, Liang Zhao^{1†}, Michio Tateno², Omar A. Saleh^{1,2,3},

Zvonimir Dogic^{1,4}, M. Cristina Marchetti^{1,4*}

*Corresponding author: mcmarche@physics.ucsb.edu

†These authors contributed equally to this work.

This PDF file includes:

Supplementary Text

Figures S1 to S3

Tables S1 to S4

Captions for Movies S1 to S2

Captions for Data S1 to S2

Other Supplementary Materials for this manuscript:

Movies S1 to S2

Supplementary Text

Capillary length measurement

The capillary lengths l_c between the PEO and dextran phase were measured using a previously published method (32). Passive samples containing no MT or KSA and containing 1.8%-2.0% PEO and 1.8%-2.0% dextran were placed in transparent fluorinated ethylene propylene (FEP) tubes with inner diameters 2.4 mm. The samples were centrifuged at 2000 g relative centrifugal force for 1 min (Fisher Scientific, 05-090-128) to bulk separate the PEO-rich and dextran-rich phases. The samples were then imaged on a laser sheet microscope (Zeiss Z.1 Lightsheet). The dextran phases de-wetted the FEP wall (Fig. S1 A). The interface profiles near the wall were then fitted by exponential functions to obtain l_c (Fig. S1 B).

Gravity effect on bicontinuous structure

In the experiment, since the dextran phase has a slightly larger density than the PEO phase, it gradually sediments in the $-z$ direction due to gravity over time. This causes an inhomogeneous amount of dextran phase at different z positions (Fig. S3 B, C). To minimize this effect, we define the area fraction of the dextran phase at each z as

$$\phi_{2D}(z) = A_d(z)/A_{total}(z) \quad (S1)$$

where $A_d(z)$ is the area of dextran phase and $A_{total}(z)$ is the area of the whole sample. In each sample, we pick the z position where $\phi_a - 0.05 < \phi_{2D}(z) < \phi_a + 0.05$ (Fig. S3 A) for all analysis.

To verify that the bicontinuous structure persists in steady state, we image the sample at $t=10$ min, 40 min, 120 min and 180 min (Fig. S4). In each acquisition, we image the sample for 5 min, and we keep the sample on a rotor at 24 rpm between the acquisitions. We observe the bicontinuity persists and w_a remains the same over 2 hours (Fig. S4), which reveals that the sample is in steady state in absence of sedimentation, consistent with simulation results (Fig. 1 B).

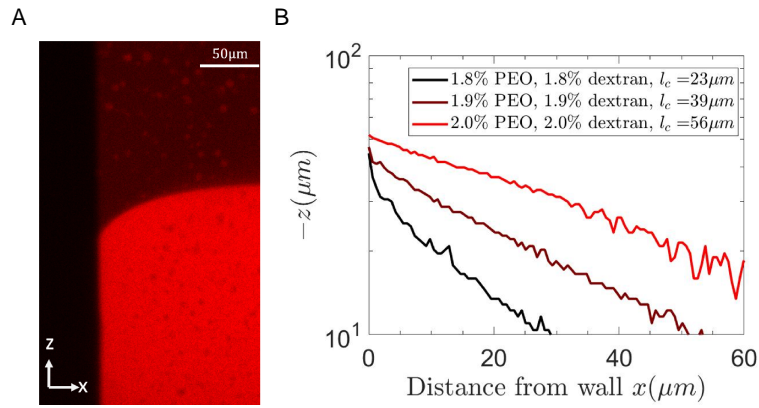


Figure S1: Measurement of capillary lengths between the two separated phases. (A) A two-dimensional crosssection of the interface profile between two bulk separated phases near the wall in a static sample containing 1.9% PEO and 1.9% dextran. The dextran phase de-wets the FEP wall. (B) The interface height z versus distance from the wall x plotted on a log-linear scale, demonstrating the exponential dependence of the height near the wall. The capillary lengths of the samples with three different polymer concentrations are $23\text{ }\mu\text{m}$, $39\text{ }\mu\text{m}$, and $56\text{ }\mu\text{m}$ each. The values are obtained by fitting an exponential function to the interface profile near the wall. The measured samples contain no MTs or KSA.

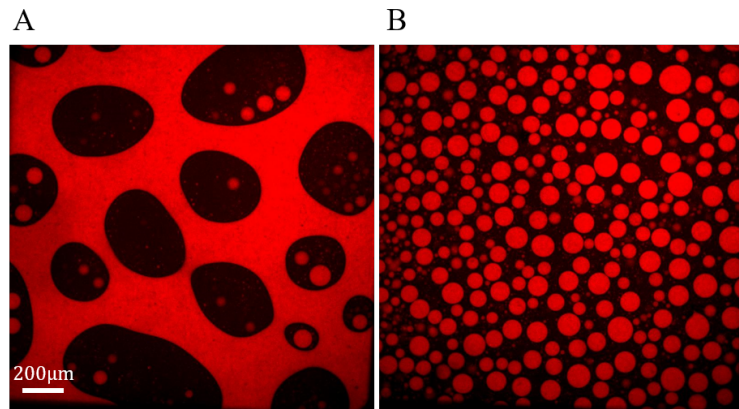


Figure S2: Passive phase separated samples form droplets (A,B) Two dimensional crosssections of passive samples with initially 1.8% PEO and 1.8% dextran, no KSA. The passive phase forms droplets when $\phi_a = 0.56 > 0.5$ in (A) and the active phase form droplets when $\phi_a = 0.41 < 0.5$ in (B).

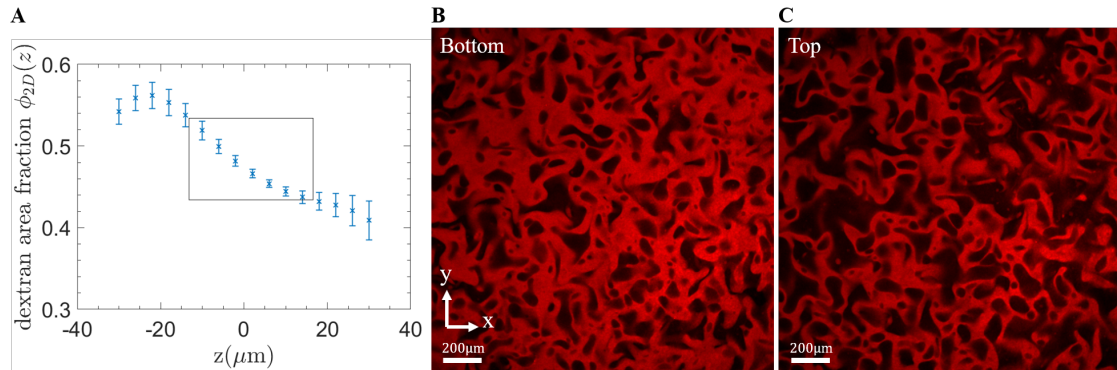


Figure S3: Gravity causes inhomogeneous dextran phase fraction at different z positions. (A) Dextran area fraction ϕ_{2D} vs. z , averaged over 5 minutes. $z = 0$ is the middle of the sample. The gravitational field points along negative z . The volume fraction of dextran phase $\phi_a = 0.48$. The black box indicates where $\phi_a - 0.05 < \phi_{2D}(z) < \phi_a + 0.05$. (B, C) 2D horizontal cross-sections of the sample in (A) at $t = 2.5$ min and z position where $\phi_{2D}(z) = \phi_a + 0.05$ (B) and $\phi_{2D}(z) = \phi_a - 0.05$ (C). The sample has an initial concentration of 42 nM KSA, 1.8% PEO and 1.8 % dextran.

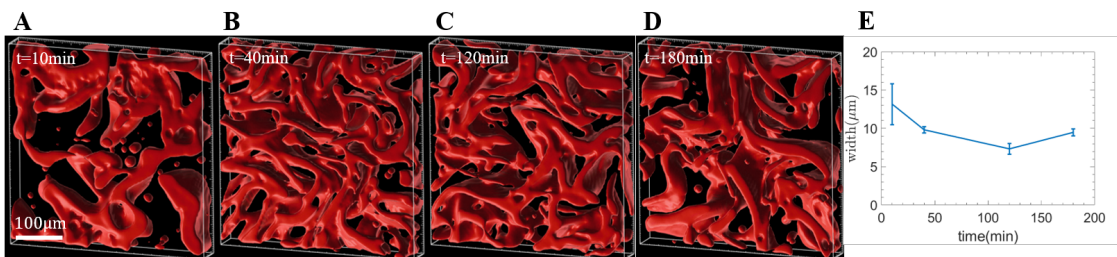


Figure S4: Bicontinuous structure reached steady state. 3D visualizations of the dextran phase (red) at 4 different time points (A-D). The network structure reached a steady state at $t = 40$ min and remained similar over 2 hours (B-D) together with the active width w (E). The sample initially contain 92 nM KSA, 1.8% PEO and 1.8% dextran and is recombined to obtain active fraction $\phi_a = 0.28$.

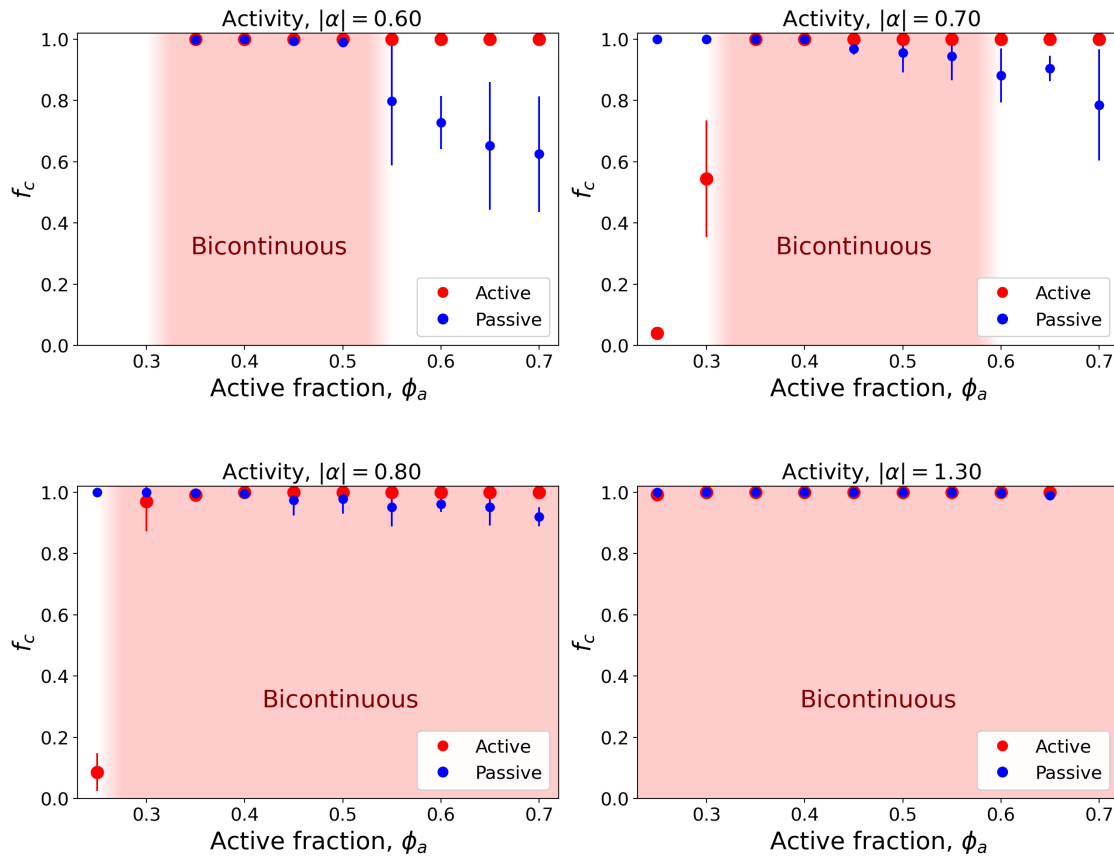


Figure S5: Bicontinuity for increasing activity The dependence of active/passive domain connectedness fractions on the activity. For large activities, the bicontinuous state for the entire range of volume fractions explored numerically i.e. the spinodal region of the passively phase separating system.

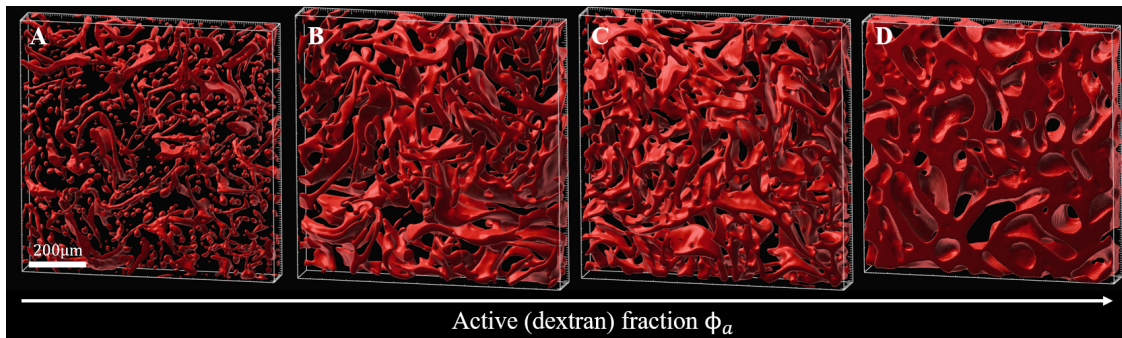


Figure S6: Visualization of active phase (red) morphology over varying ϕ_a . Samples contain $\phi_a = 0.16$ (A), 0.29 (B), 0.38 (C), 0.60 (D), corresponding to data points in Fig. 2 D. All samples initially contain 183 nM KSA , 1.8% PEO, and 1.8% dextran and are recombined to obtain various ϕ_a .

Caption for Movie S1. Three-dimensional visualization of active phase (red) forming a dynamic network in experiment. The movie starts at 1.5 h after the sample was prepared. The sample initially contains 1.9% PEO, 1.9% dextran, 183 nM KSA.

Caption for Movie S2. Three-dimensional visualization of active phase (red) forming a dynamic network in simulation. The sample is same as Fig. 1 A-B.